OPEN

Correspondence and
requests for materials
should be addressed to
J.H.W. (jhwei@whu.
edu.cn)

Quick and Facile Preparation of Visible light-Driven TiO$_2$ Photocatalyst with High Absorption and Photocatalytic Activity

Yucheng Yang, Ting Zhang, Ling Le, Xuefeng Ruan, Pengfei Fang, Chunxu Pan, Rui Xiong, Jing Shi & Jianhong Wei

Key Laboratory of Artificial Micro- and Nano-structures of Ministry of Education and School of Physics and Technology, Wuhan University, Wuhan 430072, China.

Self-doping TiO$_2$ has recently attracted considerable attention for its high photocatalytic activity under visible-light irradiation. However, the literature reported synthetic methods until now were very time-consuming. In this study, we establish a quick and facile method for obtaining self-doping TiO$_2$ with the use of directly treated commercial P25 at a desired temperature for only 5 min through spark plasma sintering technology. With the using of this method, the modified P25 samples exhibit significantly high photoelectric and photocatalytic performance. Furthermore, the sample prepared at 600°C exhibits the optimum catalytic activity. The photodegradation and H$_2$ evolution rates of this samples are significantly higher than those of unmodified P25 sample under visible-light irradiation. The physical origin of the visible-light absorption for the modified P25 samples is investigated in detail according to their structural, optical, and electronic properties. This work will provide a quick and facile method for the large-scale synthesis of visible-light driven photocatalyst for practical applications.

Semiconductor photocatalytic materials show great potential in solving the problems associated with energy shortage and environmental pollution because of their unique advantages, such as the oxidative decomposition of organic pollutants, splitting of water into hydrogen gas, CO$_2$ conversion, heavy-metal ion reduction, as well as deodorant, antisepsis, and sterilization properties, etc[1-4]. Up to now, considerable effort has been exerted to develop efficient sunlight-activated photocatalysts such as BiFeO$_3$, g-C$_3$N$_4$, graphene oxide, Ag-BiPO$_4$, Cu$_2$ (OH) PO$_4$, and Bi$_2$WO$_6$[5-10]. Among these photocatalysts, TiO$_2$ has emerged among the most fascinating materials and has thus gained in capturing the attention of physical chemists, physicists, and material scientists for its inertness to chemical environments, long-term photostability and non-toxicity. However, the large band gap (3.0 eV for rutile and 3.2eV for anatase) and low quantum efficiency of TiO$_2$ have limited its practical application.

Several approaches have been used to modify the TiO$_2$ semiconductor by enlarging its spectral response range and improving its quantum efficiency. These approaches include transition metal[11] or nonmetal[12,13] doping, noble metal loading[14], semiconductor compounding[15-17], and organic dye sensitizing[18]. Chen et al. recently reported that disorder-engineered TiO$_2$ nanocrystals (black TiO$_2$) prepared by hydrogenating TiO$_2$ nanocrystals at 20 bars H$_2$ atmosphere for approximately 5 days exhibited substantial solar-driven photocatalytic activities, including the photo-oxidation of organic molecules in water and the production of hydrogen with the use of a sacrificial reagent[19]. Since then, studies on black TiO$_2$ or self-doping TiO$_2$ have attracted widely attention[20-27]. However, most synthetic methods reported in these references are time-consuming or need to use hydrogen as reactant. Thus, developing a more economical method to obtain TiO$_2$ photocatalyst with higher catalytic activity is desirable.

In this study, we reported a facile method for obtaining self-doping TiO$_2$ with the use of directly treated commercial P25 at a desired temperature X (X= 300, 400, 500, 600, 700, or 800)°C for only 5 min through spark plasma sintering (SPS). For sake of simplicity, the samples were called as SPS-TX, according to the desired temperature X.

SPS technology reportedly has several obvious advantages, so, we believe this approach can overcome the limitations of previous methods. The first feature is that the vacuum and reducing atmosphere of SPS sintering furnace can achieve a satisfactory reduction effect through long-time hydrogen treatment within a short period while avoiding the dangers of hydrogen explosion. We attempted to treat commercial P25 at 600°C for 5, 30, and

60 min with the use of SPS technology. The sample treated for 5 min can obtain similar photocatalytic activity as that treated for 30 min or longer (omitted here). The second feature is that high frequency direct current plasma glow discharge can activate the samples, thus producing amounts of hydroxyl radicals and atomic oxygen or oxygen-free radicals[28,29]. This effect is beneficial to photocatalytic activity. With the above consideration, we prepared a series of SPS-modified P25 samples.

Results

We investigated the phase structure, color, and morphology of different samples using X-ray diffraction (XRD), a digital camera, and transmission electron microscopy (TEM), respectively (Figure 1). The XRD patterns (Figure 1a), show that the P25 and SPS-T300, SPS-T400, and SPS-T500 samples show a mixture of rutile and anatase phase structures. However, the anatase contents are gradually decreased with increasing heat-treatment temperature. Meanwhile, the SPS-T600 sample only exhibited an XRD pattern corresponding to rutile TiO_2 (PDF No. 21-1276), and no anatase peak was observed. The XRD patterns of SPS-T700 and SPS-T800 were similar to those of SPS-T600. The crystallite size can also be determined from the broadening of the corresponding X-ray spectral peaks using the Scherrer formula: $d = k\lambda/\beta \cos \theta$, where d is the crystallite size, λ is the wavelength of the X-ray radiation (CuKα = 0.1542 nm), k is usually taken as 0.89, and β is the line width at half-maximum height. The calculation results are shown in Table 1.

Figure 1b shows that the as-prepared samples exhibit a series of color changes from white to gray and then to light black when the SPS

temperature changes from 300°C to 800°C. The controlled morphologies of P25 and SPS-T600 are shown in Figures 1c and 1d. P25 is nearly spherical with diameter of approximately 20 nm. After treatment with SPS technology at 600°C for 5 min (for SPS-T600 sample), the shape of P25 became irregularly spherical with diameter reaching 70 nm–90 nm. The results are consistent with those of XRD analysis.

Discussion

Different heat-treatment temperatures enable the fine adjustments of optical properties, as indicated by the ultraviolet-visible absorption spectra (Figure 2a). The absorption edge moves toward longer wavelengths, which indicates a decreasing band gap from the SPS process (Figure 2b). The optical band gap of the modified P25 is 3.05 eV, whereas that of SPS-T600 is estimated to be ~2.58 eV. This band gap is sufficient for absorption in the visible-light range. The optical band gaps of the other samples are shown in Table 1.

The photocurrent (I)-time (t) response was used to detect the transient photocurrent responses and to provide evidence for the electron-hole transfer mechanism. The typical I-t response curves for different samples with several on-off cycles under visible light irradiation are shown in Figure 3a. The heat-treatment temperature significantly influenced the photocurrent (Figure 3a). The photocurrent of SPS-modified samples initially increased and then decreased with increasing heat-treatment temperature from 300°C to 800°C. The optimum heat-treatment temperature for the SPS process was 600°C. The photocurrent of the SPS-T600 sample was approximately 10 times higher than that of the P25 samples. The
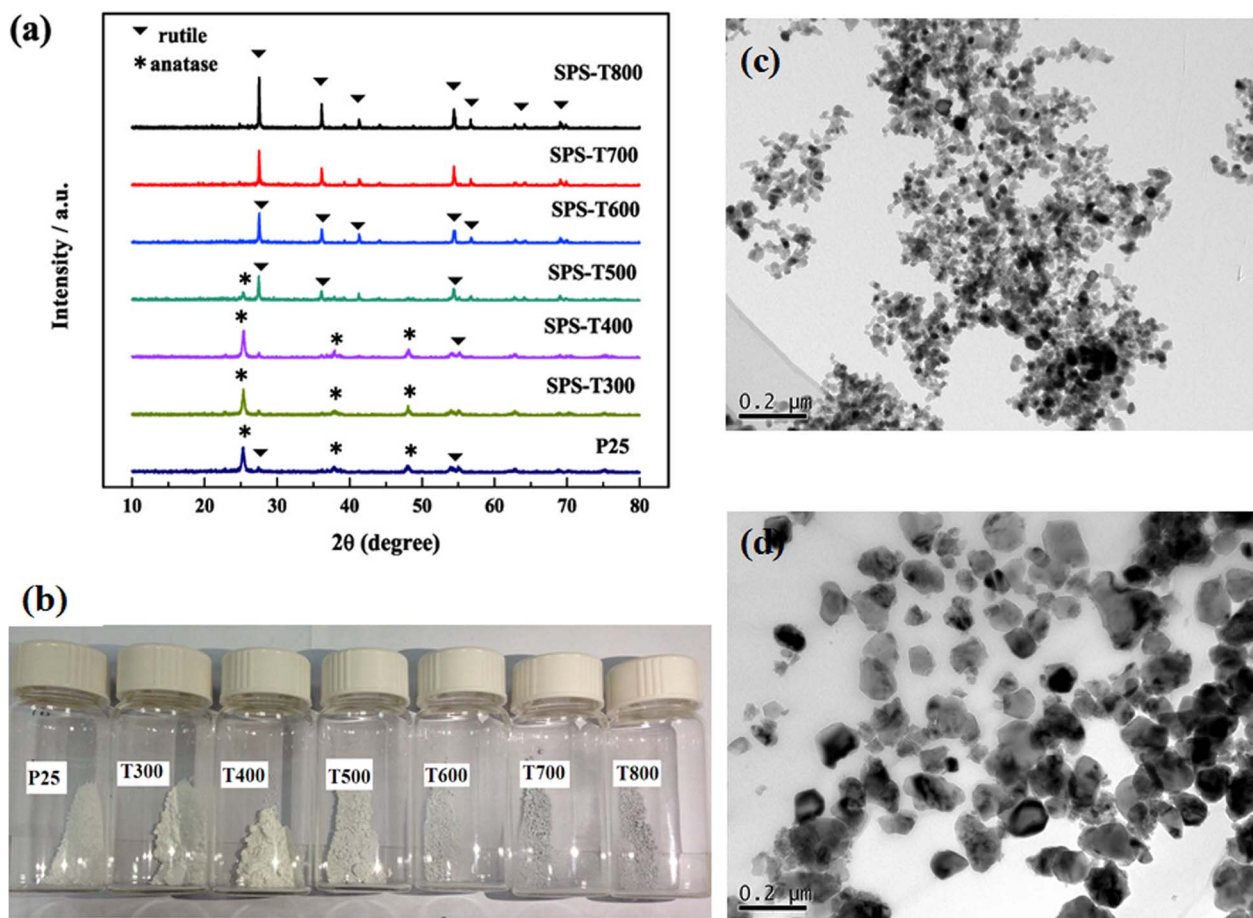

Figure 1 | (a) XRD patterns of P25 and modified P25 powders after heat treatment at 300°C to 800°C for 5 min in an SPS furnace. (b) Digital photos of P25 and modified P25 powders. (c) TEM image of P25. (d) TEM image of SPS-T600.

Table 1	The particle size and band-gaps of different samples						
Sample	P25	SPS-T300	SPS-T400	SPS-T500	SPS-T600	SPS-T700	SPS-T800
Particle Size	20.6 nm	23.4 nm	32.5 nm	61.3 nm	75.5 nm	90.4 nm	97.1 nm
Bandgap	3.05 eV	2.97 eV	2.95 eV	2.69 eV	2.58 eV	2.78 eV	2.88 eV

obvious enhancement of SPS-T600 in the photocurrent indicated more efficient separation of photogenerated electrons or holes and less recombination of the charge carrier at the interface.

Electron paramagnetic resonance (EPR) spectroscopy, a highly sensitive method that detects unpaired spins, was employed to examine the Ti^{3+} and oxygen vacancies. As shown in Figure 3b, the untreated P25 contains almost completely contained Ti^{4+} ($3d^0$) and showed weak unpaired electrons signals. For SPS treated samples, a strong EPR signal was observed at g = 1.958, which was characteristic of paramagnetic Ti^{3+} centers. Ti^{4+} may have trapped the electrons that the SPS process produced, thus further reducing Ti^{4+} to the Ti^{3+} state ($Ti^{4+} + e \rightarrow Ti^{3+}$). In addition, an oxygen loss from the surface of TiO_2 usually accompanies this process. Such loss results in numerous oxygen vacancies ($O^{2-} - e \rightarrow O^-$) in modified P25[30,31]. Furthermore, EPR signal intensity initially increases with increasing treatment temperature up to 600°C. Thereafter, the signal intensity sharply declines with a further increase in heat-treatment temperature up to 700°C and 800°C. The strongest EPR signal is obtained at SPS-T600, which indicates that the SPS-T600 sample generated the largest amount of Ti^{3+} and oxygen vacancies. In addition, the amount of Ti^{3+} and oxygen vacancies may introduce mid-gap states, which can form a continuum extending to and overlapping with the valence band (VB) or conduction band (CB) of TiO_2 as the capture of photoelectrons[22,32,33] correspondingly leads to a narrow band gap (Figure 4d) and visible-light photocatalytic activity. Another potential advantage of these Ti^{3+} and oxygen vacancies is that they provide trapping sites for photogenerated carriers and thus prevent these carriers from rapid recombination, thereby promoting electron transfer and photocatalytic reaction.

The photoluminescence (PL) technique detected the concentration of ·OH radicals on the sample surface with the use of terephthalic acid as a probe molecule, which readily reacted with ·OH radicals to produce a highly fluorescent product. The PL intensity of 2-hydro-xyterephtalic acid is proportional to the amount of ·OH produced on the surface of TiO_2[34].

Figure 3c shows the change in the PL spectra with irradiation time for SPS-T600 samples in terephthalic acid solution. A gradual increase in PL intensity at approximately 425 nm is observed with increasing irradiation time. However, no PL increase is observed in the absence of visible light on SPS-T600 samples. This result suggests that the fluorescence stems from the chemical reactions between terephthalic acid and ·OH formed at the SPS-T600/water interface through photocatalytic reactions.

Figure 3d shows the change in PL spectra with irradiation time for P25 and modified P25 samples. At a fixed time of 60 min, the formation rate of OH radicals on the modified P25 samples initially increased gradually and then decreased with increasing heat-treatment temperature. The SPS-T600 sample still shows the strongest PL signal. The result can be attributed the large amounts of unpaired electrons and holes on the surface of the SPS-T600 samples, as shown in the results of the I-T and ESR spectra. The surface, which adsorbed O_2 and H_2O to form more ·OH radicals, easily accepts electrons and holes.

The photocatalytic activity of different samples was evaluated by measuring the time-dependent degradation of methylene blue (MB) under UV-light irradiation (Figure S1, ESI) and visible-light irradiation (Figure 4a). From Figure 4a, we can see that the unmodified P25 sample shows poor photocatalytic activity in the visible-light range. The degradation rate constant k is ~0.0076/min, which is attributed to the large band gap energy of TiO_2. For the SPS modified samples, the photodegradation activity at the same time period increases with increasing rutile ratio, which in turn increase with increasing heat-treatment temperature (from 300°C to 600°C). The photodegradation rate constant k reaches the maximum ~ 0.1007/min when P25 completely transfers into the rutile phase (at 600°C). This value is approximately 13.25 times higher than that
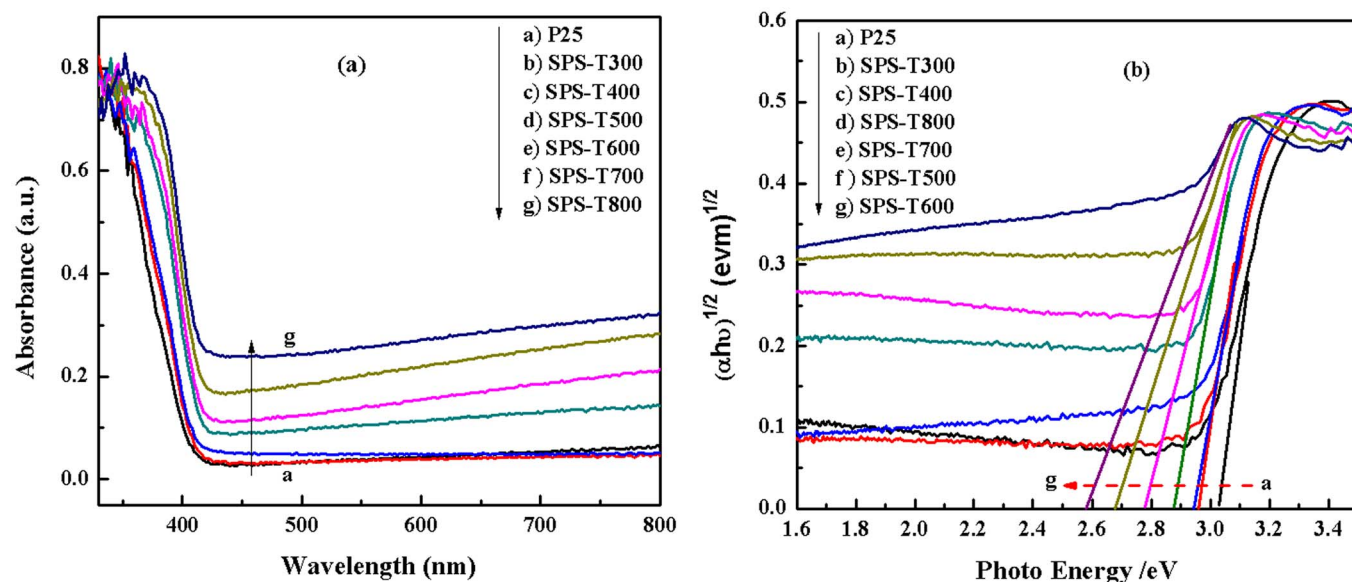

Figure 2 | (a) Ultraviolet–visible diffuse reflectance spectra of P25 and modified P25 powders after heat treatment at 300°C to 800°C for 5 min in an SPS furnace. (b) $(\alpha h\nu)^{1/2}$ as a function of photon energy, where α is the absorption coefficient, and the intercepts of extrapolated straight line give the corresponding direct band gaps of P25 and modified P25 powders.
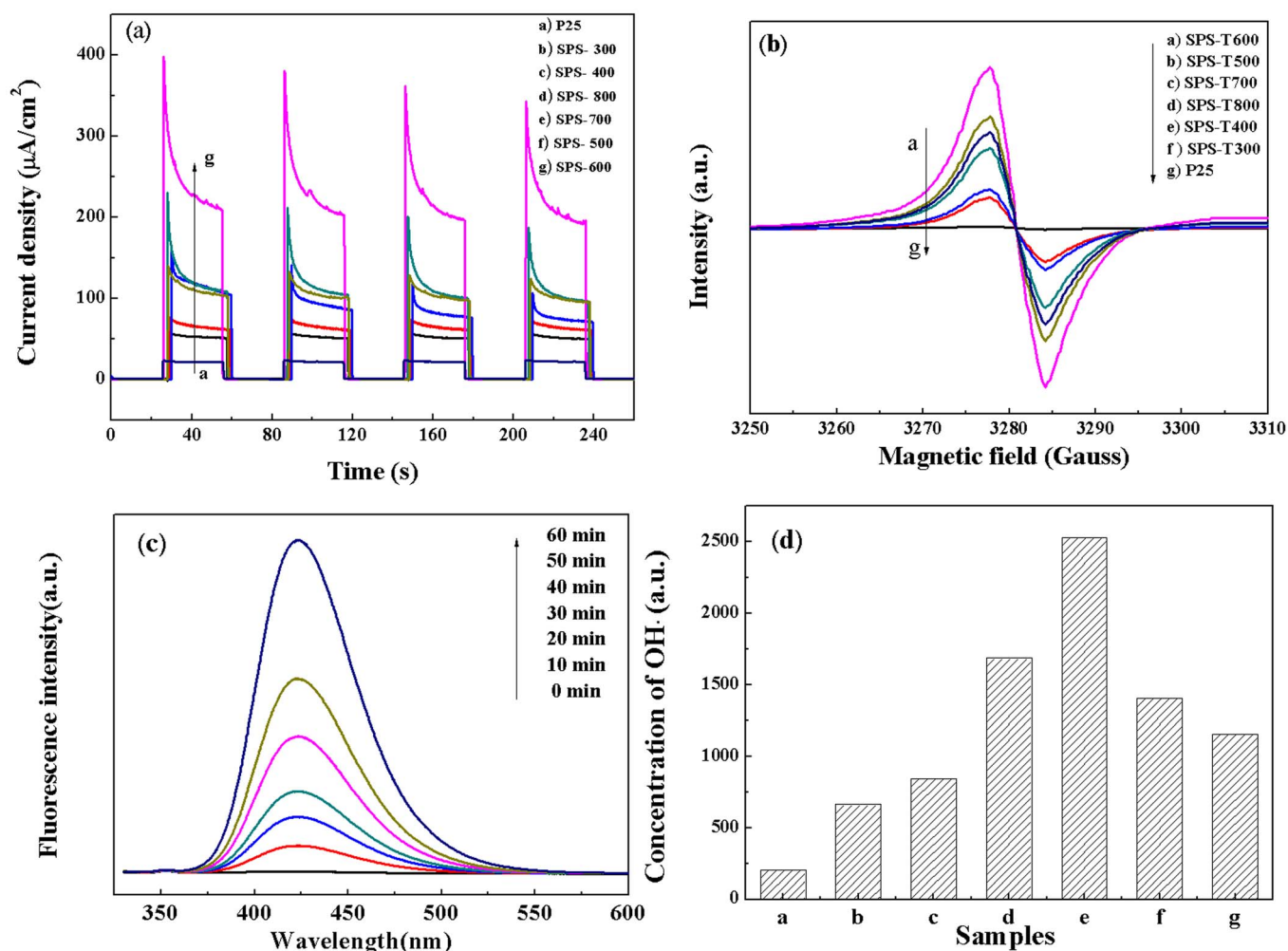
Figure 3 | (a) Photocurrent generation on the catalyst electrodes coated with P25 and modified P25 samples; $[Na_2SO_4]$ = 0.5 M; $\lambda > 420$ nm, continuously N_2 purged. (b) ESR spectra of P25 and modified P25 powders after heat treatment at300°C to 800°C for 5 min in an SPS furnace. (c) Fluorescence spectral changes in 5×10^{-4}M NaOH solution of terephthalic acid for SPS-T600. (d) Change in PL spectra with irradiation time for P25 and modified P25 samples at a fixed time.

of unmodified P25 under visible-light irradiation. Thereafter, the photodegradation rate constant decreases with further increases in heat-treatment temperature. This result may be attributed to the further increase in the particle sizes and stability of structures with increasing heat-treatment temperature to 700°C and 800°C. This condition consequently results in the reduction of the active sites per unit area as well as lower photocatalytic activity.

Photocatalytic water splitting H_2 production from aqueous methanol solution over the as-prepared SPS-T600 and P25 samples was used to evaluate photocatalytic activity. A typical time course of H_2 production is shown in Figure 4b ($\lambda > 420$ nm, a 300 W xenon lamp with a 420 nm cut-off filter). The H_2 production rate constant k of SPS-T600 is ~61.2μmol/0.1 g/h, which is approximately 9.45 times higher than that of unmodified P25 under visible light irradiation.

To evaluate the photochemical stability of the SPS-T600 catalyst, cyclic stability tests on MB solution degradation and H_2 evolution were examined, as shown in Figures 4 b and 4c. Both show that the photocatalytic activities are maintained without a noticeable decrease after recycling five times, which demonstrates the excellent stability of the SPS-T600 sample. This result is significant from the perspective of practical applications because the enhanced photocatalytic activity and prevention of catalyst deactivation will result in more cost-effective operations.

Normal rutile nanoparticles generally show weak photocatalytic activity. However, the rutile TiO_2 nanoparticles obtained from SPS

technology show broad, red-shifted absorption bands in the visible-light region and exhibit high visible-light-induced photocatalytic activity. What reason is this cause? In general, the performance of the photocatalyst depends on a series of parameters, such as surface area, adsorption capacity, optical absorption, carrier recombination rate, oxygen vacancy and Ti^{3+} formation[35–38]. The adsorption capacity of the sample depends to a large extent on its surface area or particle size. The smaller particle size in most cases corresponds to a larger surface area and stronger adsorption capacity. In our case, the particle sizes of SPS-T600 are bigger than those of P25. Thus, the influence of specific surface area of the product is negligible. The analysis means that the adsorption capacities of modified P25 samples are not the main factor to induce higher photocatalytic activity.

Secondly, taking into account the optical properties. With increasing heat-treatment temperature, although modified P25 samples' absorption in the visible region increased, the corresponding absorption in the UV range haven't obvious change. Therefore, the SPS effect on the optical properties of P25 is limited to visible light range. This result refers that the optical properties are also not the main factor to induce higher photocatalytic activity of modified P25 samples.

Now that both of the above were not the main influence factors of the photocatalytic activity, the main cause may be attributed to the following two factors: First, the SPS-treated process results in the production of Ti^{3+} and O^-, which introduces continuous states
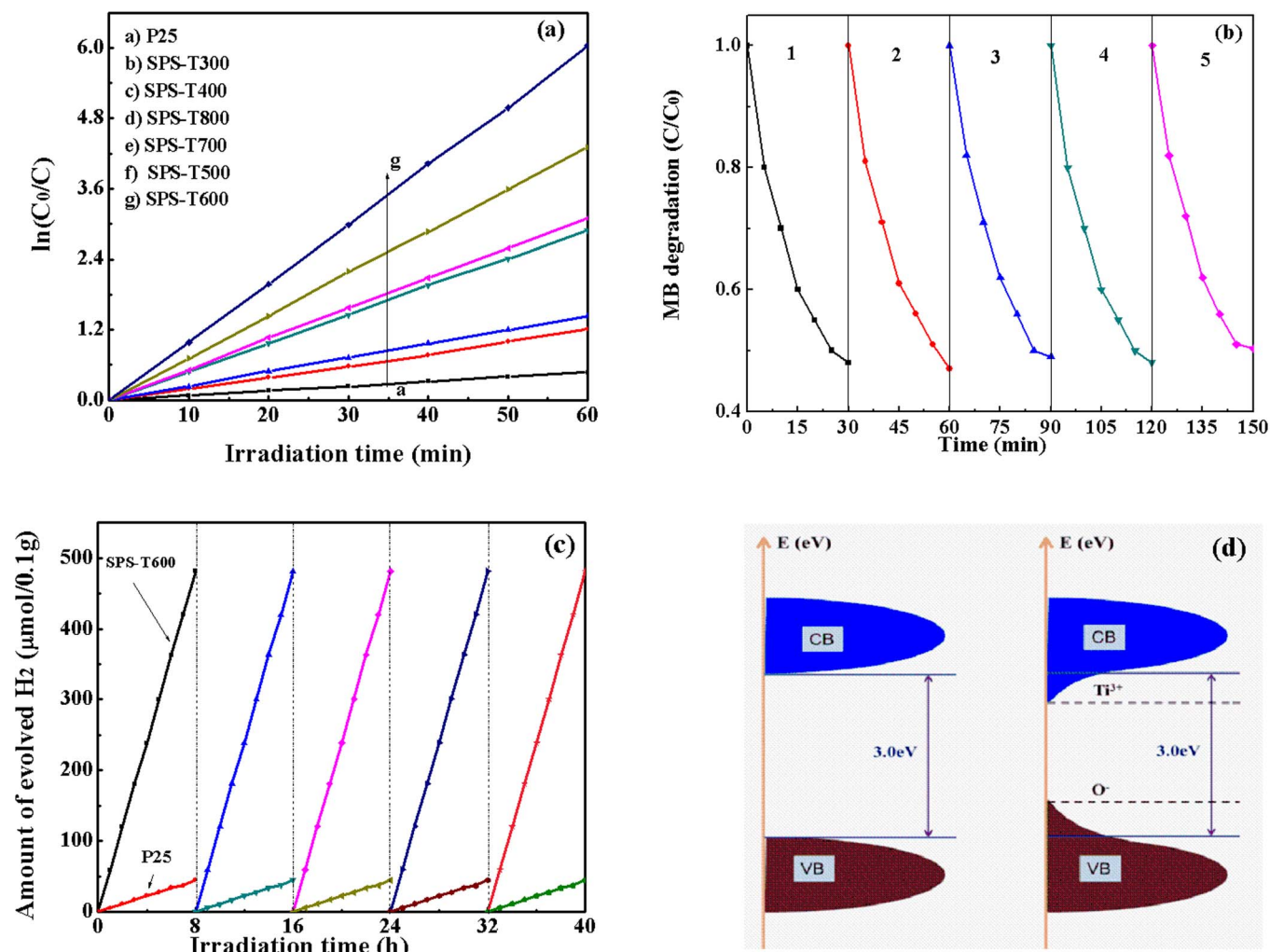
Figure 4 | (a) Visible light-driven photocatalytic degradation of methylene blue (MB) using P25 or modified P25 powders. (b) Recyclability of the SPS-T600 for the degradation of MB under visible light irradiation. (c) Stable hydrogen evolution from water using P25 and SPS-T600 under visible light irradiation ($\lambda > 420$ nm) (A typical time courses of H_2 production from water containing 10 vol.% methanol as an electron donor). (d) Proposed energy band diagram scheme of SPS-T600.

between the VB and CB of TiO_2 with the capture of photoelectrons, which in turn results in a narrow band gap and high visible-light photocatalytic activity. Second, compared with that of the unmodified P25 sample, the surface of the modified P25 samples exhibited more separated electrons, holes, and ·OH radicals. These electrons, holes, and ·OH radicals will participate in the photocatalytic reaction. Thus, SPS-treated samples show higher photocatalytic activity than unmodified P25 sample. The highest photocatalytic activity found in SPS-T600 is an optimization of all the factors discussed above.

The SPS-T600 sample exhibited optimum visible-light-induced photocatalytic activity and high recycling stability upon light irradiation. The degradation rate constant of the SPS-T600 sample was significantly higher than that of P25. This study provides a simple and economic method for the large-scale synthesis of a highly active photocatalyst for practical applications.

Methods

Sample preparation. P25 was purchased from the Degussa Company. In a typical SPS heat-treatment process, 1.0 g of P25 powders was loaded into a cylindrical carbon die with an inner diameter of 15 mm. The die was then sintered in vacuum in an SPS apparatus (SPS-3.20 MKII, Sumitomo Coal Mining Co. Ltd., Tokyo, Japan). The temperature was raised to the desired temperature (300°C, 400°C, 500°C, 600°C, 700°C, or 800°C) over a period of 4 min. The sample was then heated at the desired temperature for 5 min under 60 MPa. Thereafter, the sample was naturally cooled to

room temperature in a furnace. During the sintering process, the sample temperature was measured using an infrared camera through a hole in the middle of the cylindrical carbon die. The modified P25 sample after heat treatment at 300°C to 800°C for 5 min is denoted as SPS-TX (X= 300–800).

Physical Characterization. The crystal structures were determined using powder X-ray diffraction (XRD), on a D8 advance X-ray powder diffractometer (Germany) with CuKα radiation ($\lambda = 0.1542$ nm). Particle sizes and surface morphology were observed with a JEOL JEM-2010 TEM, (Japan) at an accelerating voltage of 200 kV. The UV-vis diffuse reflectance spectra of the samples were obtained using an UV-vis spectrophotometer (Cary 5000 UV-vis-NIR, Australia) with an Integrated Sphere Attachment. The absorption spectra were then obtained from the reflectance spectra through Kubelka-Munk transformation.

Photoelectrochemistry characterization. The photocurrents were measured using an electrochemical analyzer (CHI660A, CH Instruments Co.) in a standard three-electrode system with as-prepared samples as the working electrode, a saturated calomel electrode as reference, and a platinum wire parallel to the working electrode as a counter electrode. A Xe lamp (350W) positioned 10 cm away from the working electrode was used as the light source. An ultraviolet cutoff filter was applied to cut off UV light ($\lambda < 420$ nm). Photocurrent as a function of time was measured in aqueous $NaSO_4$ (0.5 M) solution under visible-light irradiation. Electrochemical impedance spectroscopy (EIS) measurements were conducted in the above configuration of cell under irradiation ($\lambda > 420$ nm) and in a frequency range between 1 MHz and 0.1 Hz with applied biases that are equal to −0.5 V. All measurements were conducted at room temperature under an N_2 atmosphere to obtain highly reproducible data. The magnetic resonance measurements were performed with a Bruker 300 ESP ESR spectrometer operating at the X-band 9.5 GHz.

Analysis of hydroxyl radicals (·OH). The PL technique detected the formation of ·OH radical on the sample surface using terephthalic acid as a probe molecule, which readily reacted with ·OH radicals to produce highly fluorescent products. This method relies on the PL signal at 425 nm of 2-hydroxyterephthalic acid. The PL intensity of 2-hydroxyterephthalic acid is proportional to the concentration of ·OH produced on the surface of TiO_2. The experimental procedures were as follows: at ambient temperature, 0.1 g of powder sample was dispersed in 20 ml of the 5×10^{-4} M terephthalic acid aqueous solution with a concentration of 2×10^{-3} M NaOH in a dish having a diameter of approximately 9.0 cm. A 125 W high-pressure Hg lamp (10 cm above the dishes) was used as a light source. The integrated visible-light intensity measured with a visible-light radiometer (Model: FZ-A, made in Photoelectric Instrument Factory of Beijing Normal University) was 2.9 ± 0.1 mW/cm^2 with a wavelength range of 400 nm–1000 nm. The PL spectra of the generated 2-hydroxyterephthalic acid were recorded using a Hitachi F-4600 fluorescence spectrophotometer. After irradiation every 10 min, the reaction solution was filtrated to measure the increase in the PL intensity at 425 nm.

Organic dye decomposition. A self-made cylindrical glass vessel with a water-cooling jacket was used as a photochemical reactor. The photocatalytic activities of the as-prepared samples were evaluated through the degradation of a model MB pollutant dye solution. The optical system for the photocatalytic reactions was composed of a 350 W xenon arc lamp and a cutoff filter ($\lambda > 420$ nm) at room temperature. In which, a 100 mL of MB solution with an initial concentration of 10 mg/L in the presence of solid catalyst (50 mg) was stirred in the dark for 30 min to achieve good dispersion and adsorption equilibrium. Then, the mixed solution was illuminated by the xenon arc lamp 10 cm away. With 30 min intervals of illumination, MB was analyzed at 660 nm as a function of time on a UV-vis spectrophotometer (Model: Shimadzu 2450/2550 PC). The SPS-600 samples were repeatedly used for five times under the same experiment conditions to test the photocatalytic stability.

Photocatalytic H_2 generation. A photocatalyst (100 mg) loaded with Pt (0.5 wt.%) was placed into an aqueous methanol solution (50 mL, 40%) in a closed-gas circulation system. An AM 1.5 solar power system was used as the light irradiation source. Methanol was used as a sacrificial reagent. The P25 and SPS-600 samples were repeatedly used for five times under the same experiment conditions to test the photocatalytic stability.

1. Fresno, F., Portela, R., Suarez, S. & Coronado, J. M. Photocatalytic materials: recent achievements and near future trends. *J. Mater. Chem. A* **2**, 2863–2884 (2014).
2. Luo, J. S. *et al.* Water photolysis at 12.3% efficiency via perovskite photovoltaics and earth-abundant catalysts. *Science* **345**, 1593–1596 (2014).
3. Nebel, C. E. Photocatalysis: A source of energetic electrons. *Nature Mater.* **12**, 780–781 (2013).
4. Lang, X. J., Chen, X. D. & Zhao, J. C. Heterogenerous visible light photocatalysis for selective organic transformations. *Chem. Soc. Rev.* **43**, 473–486 (2014).
5. Wang, X. C. *et al.* A metal-free polymeric photocatalyst for hydrogen production from water under visible light. *Nature Mater.* **8**, 76–80 (2009).
6. Huo, Y. N., Miao, M., Zhang, Y., Zhu, J. & Li, H. X. Aerosol-spraying preparation of a mesoporous hollow spherical $BiFeO_3$ visible photocatalyst with enhanced activity and durability. *Chem. Commun.* **47**, 2089–2091 (2011).
7. Dong, F. *et al.* In Situ Construction of g-C_3N_4/g-C_3N_4 Metal-Free Heterojunction for Enhanced Visible-Light Photocatalysis. *ACS Appl. Mater. Interfaces* **5**, 11392–11401 (2013).
8. Fulekar, M. H. *et al.* Ag incorporated nano $BiPO_4$: sonochemical synthesis, characterization and improved visible light photocatalytic properties. *RSC Adv.* **4**, 10097–10107 (2014).
9. Wang, G. *et al.* $Cu_2(OH)PO_4$, a Near-Infrared-Activated Photocatalyst. *Angew. Chem. Int. Ed.* **52**, 4810–4813 (2013).
10. Tian, J. *et al.* A Bi_2WO_6-Based Hybrid Photocatalyst with Broad Spectrum Photocatalytic Properties under UV, Visible, and Near-Infrared Irradiation. *Adv. Mater.* **25**, 5075–5080 (2013).
11. Cai, Y. Q., Bai, Z. Q., Chintalapati, S., Zeng, Q. F. & Feng, Y. P. Transition metal atoms pathways on rutile TiO_2 (110) surface: Distribution of Ti^{3+} states and evidence of enhanced peripheral charge accumulation. *J. Chem. Phys.* **138**, 154711 (2013).
12. Asahi, R., Morikawa, T., Ohwaki, T., Aoki, K. & Taga, Y. Visible-Light Photocatalysis in Nitrogen-Doped Titanium Oxides. *Science*, **293**, 269–271 (2001).
13. Yu, S., Yun, H. J., Kim, Y. H. & Yi, J. Carbon-doped TiO_2 nanoparticles wrapped with nanographene as a high performance photocatalyst for phenol degradation under visible light irradiation. *Appl. Catal. B: Environ.* **144**, 893–899 (2014).
14. Pradhan, Ghosh, S. D. & Chen, S. W. Janus Nanostructures Based on Au-TiO_2 Heterodimers and Their Photocatalytic Activity in the Oxidation of Methanol. *ACS Appl. Mater. Interfaces* **1**, 2060–2065 (2009).
15. Shi, J. L. On the synergetic catalytic effect in heterogeneous nanocomposite catalysts. *Chem. Rev.* **113**, 2139–2181 (2013).
16. Yang, Y. C. *et al.* Polypyrrole-Decorated Ag-TiO_2 Nanofibers Exhibiting Enhanced Photocatalytic Activity under Visible-Light Illumination. *ACS Appl. Mater. Interfaces* **5**, 6201–6207 (2013).
17. Qu, Y. Q. & Duan, X. F. Progress, challenge and perspective of heterogeneous Photocatalysts. *Chem. Soc. Rev.* **42**, 2568–2580 (2013).
18. Zhang, M., Chen, C. C., Ma, W. H. & Zhao, J. C. Visible-Light-Induced Aerobic Oxidation of Alcohols in a Coupled Photocatalytic System of Dye-Sensitized TiO_2 and TEMPO. *Angew. Chem. Int. Ed.* **47**, 9730–9733 (2008).
19. Chen, X. B., Liu, L., Yu, P. Y. & Mao, S. S. Increasing solar absorption for photocatalysis with black hydrogenated titanium dioxide nanocrystals. *Science* **331**, 746–751 (2011).
20. Wang, G. *et al.* Hydrogen-treated TiO_2 nanowire arrays for photoelectrochemical water splitting. *Nano Lett.* **11**, 3026–3033 (2011).
21. Liu, L. & Chen, X. B. Titanium dioxide nanomaterials: Self-structural modifications. *Chem. Rev.* **114**, 9890–9918 (2014).
22. Naldoni, A., Allieta, M., Santangelo, S., Marelli, M. & Fabbri, F. The effect of nature and location of defects on bandgap narrowing in black TiO_2 nanoparticles. *J. Am. Chem. Soc.* **134**, 7600–7603 (2012).
23. Huo, J. C., Hu, Y. J., Jiang, H. & Li, C. Z. In situ surface hydrogenation synthesis of Ti^{3+} self-doped TiO_2 with enhanced visible light photoactivity. *Nanoscale* **6**, 9078–9084 (2014).
24. Zhu, G. L. *et al.* Black brookite titania with high solar absorption and excellent photocatalytic performance. *J. Mater. Chem. A* **1**, 9650–9653 (2013).
25. Hamdy, M. S., Amrollahi, R. & Mul, G. Surface Ti^{3+}-containing (blue) titania: A unique photocatalyst with high activity and selectivity in visible light-stimulated selective oxidation. *ACS Catal.* **2**, 2641–2647 (2012).
26. Liao, W. J., Yang, J. W., Zhou, H., Murugananthan, M. & Zhang, Y. R. Electrochemically self-doped TiO_2 nanotube arrays for efficient visible light photoelectrocatalytic degradation of contaminants. *Electrochimica Acta* **136**, 310–317 (2014).
27. Fang, W. Z., Xing, M. Y. & Zhang, J. L. A new approach to prepare Ti^{3+} self-doped TiO_2 via $NaBH_4$ reduction and hydrochloric acid treatment. *Appl. Catal. B: Environ.* **160–161**, 240–246 (2014).
28. Liu, Y. *et al.* $CoFe_2O_4$/$BaTiO_3$ composites via spark plasma sintering with enhanced magnetoelectric coupling and excellent anisotropy. *J. Am. Ceram. Soc.* **94**, 1695–1697 (2011).
29. Wang, L., Jiang, X. & Liu, Y. Degradation of biphenyl A and formation of hydrogen peroxide induced by glow discharge plasma in aqueous solutions. *J. Hazard. Mater.* **154**, 1106–1114 (2008).
30. Zhao, Z. *et al.* Reduced TiO_2 rutile nanorods with well-defined facets and their visible-light photocatalytic activity. *Chem. Commun.* **50**, 2755–2757 (2014).
31. Wang, Z. *et al.* Visible-light photocatalytic, solar thermal and photoelectrochemical properties of aluminum-reduced black TiO_2. *Energy Environ. Sci.* **6**, 3007–3014 (2013).
32. Chen, X. B. *et al.* Properties of disorder-engineered black titanium dioxide nanoparticles through hydrogenation. *Sci. Rep.* **3**, 1510 (2013).
33. Liu, X. *et al.* Ti^{3+} self-doped TiO_{2-x} anatase nanoparticles via oxidation of TiH_2 in H_2O_2. *Catal. Today* **225**, 80–89 (2014).
34. Yu, J. G., Wang, W. G., Cheng, B. & Su, B. L. Enhancement of photocatalytic activity of Mesoporous TiO_2 powders by hydrothermal surface fluorination treatment. *J. Phys. Chem. C* **113**, 6743–6750 (2009).
35. Xia, T., Zhang, Y. L., Murowchick, J. & Chen, X. B. Vacuum-treated titanium dioxide nanocrystals: Optical properties, surface disorder, oxygen vacancy, and photocatalytic activities. *Catal. Today* **225**, 2–9 (2014).
36. Fujishima, A., Zhang, X. & Tryk, D. A. TiO_2 photocatalysis and related surface phenomena. *Surf. Sci. Rep.* **63**, 515–582 (2008).
37. Zhang, Y. L. *et al.* Structural evolution from TiO_2 nanoparticles to nanosheets and their photocatalytic performance in hydrogen generation and environmental pollution removal. *RSC Adv.* **4**, 16146–16152 (2014).
38. Zhang, Y. L. *et al.* Influence of the amount of hydrogen fluoride on the formation of (001)-faceted titanium dioxide nanosheets and their photocatalytic hydrogen generation performance. *ChemPlusChem* **79**, 1159–1166 (2014).

Acknowledgments

Author contributions

J.H.W. and Y.C.Y. conceived the concept and designed the experiment process. Y.C.Y., T.Z., L.L. and X.F.Y. performed the experiments. J.H.W., P.F.F. and C.X.P. conducted XRD, UV-vis-NIR, PL and TEM measurements. R.X. and J.S. carried out I-t and ESR characterizations; J.H.W. wrote the manuscript with contribution from all authors; everyone participated in discussions and analysis of the results.

Additional information

Supplementary information accompanies this paper at http://www.nature.com/scientificreports

Competing financial interests: The authors declare no competing financial interests.